Available online at www.sciencedirect.com

ScienceDirect

journal homepage: www.elsevier.com/locate/he

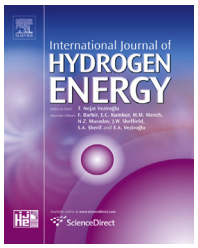

PdAu alloyed clusters supported by carbon nanosheets as efficient electrocatalysts for oxygen reduction

Wei Yan [a], Zhenghua Tang [a,b,*], Likai Wang [a], Qiannan Wang [a], Hongyu Yang [a], Shaowei Chen [a,c,**]

[a] New Energy Research Institute, School of Environment and Energy, South China University of Technology, Guangzhou Higher Education Mega Centre, Guangzhou 510006, China

[b] Guangdong Provincial Key Laboratory of Atmospheric Environment and Pollution Control, Guangdong Provincial Engineering and Technology Research Center for Environmental Risk Prevention and Emergency Disposal, School of Environment and Energy, South China University of Technology, Guangzhou Higher Education Mega Centre, Guangzhou 510006, China

[c] Department of Chemistry and Biochemistry, University of California, 1156 High Street, Santa Cruz, CA 95064, United States

ARTICLE INFO

Article history:
Received 24 June 2016
Received in revised form
25 August 2016
Accepted 7 September 2016
Available online 14 November 2016

Keywords:
PdAu alloy
Nanoclusters
Carbon nanosheets
Oxygen electroreduction
Fuel cells

ABSTRACT

PdAu alloyed clusters supported on carbon nanosheets were prepared and employed as efficient electrocatalysts for oxygen reduction reaction (ORR). PdAu clusters protected by glutathione were synthesized, while the structure and composition of the alloys were tuned through the variation of Pd-to-Au ratio. The PdAu clusters were loaded into carbon nanosheets and calcined at elevated temperature. The protecting ligands were completely removed after calcination, and uniform hybrid materials were formed. The as-prepared nanocomposites were characterized by transmission electron microscopy (TEM), scanning tunneling electron microscopy (STEM), X-ray photoelectron spectroscopy (XPS), X-ray diffraction (XRD) as well as other techniques. The composites demonstrated effective ORR activity in alkaline media. Among a series of samples, the composite with a metal mass loading of 30% and the ratio of Pd-to-Au (1:2) exhibited the highest activity, and its performance is comparable to that of commercial Pt/C, superior to PdAu clusters, carbon nanosheets as well as other supported alloyed samples, in terms of onset potential, diffusion limited current density as well as number of electron transfer. Notably, the long-term stability of the composite is markedly higher than Pt/C. The strategy can be extended for the preparation of other supported bi-metallic nanoclusters with controllable composition and optimized electrocatalytic activity for fuel cell applications.

* *Corresponding author*. New Energy Research Institute, School of Environment and Energy, South China University of Technology, Guangzhou Higher Education Mega Centre, Guangzhou 510006, China

** *Corresponding author*. Department of Chemistry and Biochemistry, University of California, 1156 High Street, Santa Cruz, CA 95064, United States

E-mail addresses: zhht@scut.edu.cn (Z. Tang), shaowei@ucsc.edu (S. Chen).

http://dx.doi.org/10.1016/j.ijhydene.2016.09.041

Introduction

Proton exchange membrane fuel cells (PEMFC) are among the most promising clean energy technologies to tackle the global energy crisis and severe environmental problems, mainly thanks to their high energy density, low operation temperature and environmental friendly reaction products [1–3]. However, the major obstacle to hinder the widespread commercialization of PEMFC is the oxygen reduction reaction occurring at the cathode, as the currently most widely employed catalyst for ORR is Pt and Pt based alloy materials, which suffer from the high price and limited supply of platinum as well as the low stability of such catalysts [4,5]. Consequently, continuous research efforts have been devoted to developing low-platinum, platinum free and non-precious metal based materials as ORR catalyst [6–14].

Alloying is a very important approach to fabricate heterogeneous catalyst, as it can provide both ensemble and ligand effects [15]. Ensemble effect is referring to atoms in certain geometric configurations can promote the catalytic process, while electronic structure of hetero metal–metal bond formation is beneficial for activation of the catalyst [15]. With the combination of the merits from two metals, the broad choice of metal elements as well as tunable surface structure and compositions, alloys have provided great opportunities for preparing desirable electrocatalyst with enhanced activity and stability. Much of the research focused on Pt alloyed nanoparticles especially Pt-transitional metals. Note that, the electronic interactions in the neighboring atoms can alter the adsorption of oxygen on the nanoparticle surface, leading to the enhancement of ORR activity. Platinum binds very strongly to oxygenated intermediates, while the induced transition metal can optimize the interaction strength with oxygenated intermediates during ORR. PtM (M = Co, Ni, Cu, Fe, etc) alloys have demonstrated superior activity than pure Pt nanoparticles [16–21]. Even if the activity requirement issue can be addressed by Pt based alloys, for ideal cathode catalyst, issues regarding stability can't be omitted and more research efforts are needed to provide valuable solutions.

Compared with Pt, palladium is not only earth abundant, but also displays remarkable catalytic activity due to the fact that Pd can form compact and stable surface oxide [22–24]. Palladium binds more strongly to oxygen than platinum while gold has little interaction with oxygen, which makes PdAu an optimal candidate to make binary alloyed nanoparticles [25]. It is largely believed that the electrocatalytic properties of PdAu alloy nanoparticles are mainly governed by their size, shape, structure as well as the local surface elemental compositions [26]. Sampath and coworkers demonstrated that the preparation of monodisperse PdAu nanoparticles with a size of 2–7.5 nm by a sol-gel reduction approach, and 200 mV positive onset potential were achieved compared to glassy carbon electrode [27]. Alloyed PdAu nanochain networks were prepared through a one-pot synthetic method by Wang and coworkers, and such networks exhibited superior ORR activity than Pd black catalyst [28]. Erikson et al. examined the electrocatalytic activity of electrodeposited PdAu alloys towards ORR in both acidic and basic electrolytes, and disclosed that the reaction mechanism of PdAu was similar to that on bulk Pd [29]. By using dodecyne as the capping agent, PdAu alloyed nanoparticles with precise composition were employed for ORR, and the best sample was identified as a Pd mass loading of 91.2%, which exhibited a mass activity over eight times than that of commercial Pt/C [25]. The above investigations indicate that PdAu alloys can be an excellent alternative for Pt-based alloyed nanoparticles.

On the other hand, to minimum the employment of the noble metals and improve the catalytic activity, a variety of supports including porous carbon [30], carbon nanosheets [31], graphene [32,33], carbon nanotubes [34] as well as other substrates [35] have been employed when using noble metal or metal alloyed nanoparticles for ORR. It has been documented that such carbon support can prevent aggregation, coalescence or decomposition during the catalytic process, meanwhile promoting the electron transfer and mass transport to facilitate the electrocatalytic reaction kinetics [32,33]. PdAu alloyed nanoparticles are promising catalysts for electroreduction of oxygen, however, to lower the employment of noble metals and enhance the catalytic activity, using carbon support might offer a feasible, cost-effective and valuable strategy to fabricate highly efficient ORR catalysts with practical application potentials. Unfortunately, to the best of our knowledge, examples have been rare to date in the case of PdAu alloyed nanoparticles. This is the primary motivation of our current investigation.

In this study, PdAu alloyed clusters supported on carbon nanosheets were prepared and employed as efficient electrocatalysts for ORR. PdAu nanoclusters protected by glutathione were synthesized, while the structure and composition of the alloys were tuned through the variation of Pd-to-Au ratio. The PdAu nanoclusters were loaded into carbon nanosheets and calcined. The ligands were completely removed after pyrolysis, and uniform hybrid materials were formed without agglomeration observed. The as-prepared nanocomposites were fully characterized by TEM, STEM, XPS and XRD. The composites demonstrated effective ORR activity in alkaline media. Among a series of samples, the composite with a metal mass loading of 30% and the ratio of Pd-to-Au (1:2) stood out as the best sample, and its performance was comparable to that of commercial Pt/C, superior to PdAu alloyed clusters, carbon nanosheets as well as other supported alloyed samples, within the context of onset potential, diffusion limited current density and number of electron transfer. Notably, such sample also exhibited remarkably higher long-term stability than commercial Pt/C.

Materials and methods

Chemicals

Hydrogen tetrachloroauric acid (III) trihydrate ($HAuCl_4 \cdot 3H_2O$) and reduced L-glutathione were obtained from Energy Chemicals (Shanghai, China), while potassium tetrachloropalladate (K_2PdCl_4) and sodium borohydride ($NaBH_4$) were purchased from Aladdin industrial Corporation (Shanghai, China). Pt/C (20 wt%, Alfa Aesar), zinc nitrate hexahydrate ($Zn(NO_3)_2 \cdot 6H_2O$, 99%, Fuchen Reagents, Tianjin), ammonium acetate (NH_4OAc, 98%, Fuchen Reagents, Tianjin),

cetyltrimethylammonium bromide (CTAB, 99%, Fuchen Reagents, Tianjin), triethylamine (TEA, 99%, Fuchen Reagents, Tianjin), methanol (99.5%, Xinyun Chemical Industry, Tianjin), and N,N-dimethylformamide (DMF, 99.5%, Fuchen Reagents, Tianjin). Water was supplied with a Barnstead Nanopure Water System (18.3 MΩ·cm). All chemicals were used as received without further purification.

Synthesis of water-soluble PdAu alloyed nanoclusters (NCs)

The synthesis of PdAu NCs was conducted by following a modified procedure in a previous report [36]. Briefly, a 10 mL aqueous solution consisting of 0.02 M $HAuCl_4 \cdot 3H_2O$ and 0.02 M K_2PdCl_4 mixtures in molar ratios of 1:0, 4:1, 2:1, 1:1, 1:2 and 0:1 was first added into a round-bottom flask under vigorous stirring (~1100 rpm). Then, a water solution containing 1.2 mmol (~6 times equivalent of the metal atoms) of L-glutathione in 10 mL pure water was added into the flask. The solution was stirred rapidly about 30 min at room temperature. Subsequently, a freshly prepared $NaBH_4$ solution (2 mmol, ~10 times equivalent of the metal atoms, dissolved in 5 mL of ice-cold water) was added to the solution immediately under vigorous stirring. The solution turned into dark red-brown in a few min. The reaction was allowed to proceed for about 3 h. The solution of PdAu NCs was dialyzed for 2 days with a semi-permeable membrane (Molecular weight cutoff = 5000 Da) for purification.

Preparation of carbon nanosheets

Carbon nanosheets were prepared by following a previously documented protocol [37,38]. Briefly, 30 mmol of $Zn(NO_3)_2 \cdot 6H_2O$ and 10 mmol of terephthalic acid were co-dissolved in 250 mL of DMF in a round bottom flask and stirred at room temperature for 3 h. Then the solution was aged at 60 °C for 72 h. After that, 50 mmol of CTAB were added into the solution, and heated at 105 °C for 90 min under magnetic stirring. Subsequently, upon the addition of TEA (0.05 mol, 6.95 mL), precipitates were formed and collected by centrifugation. The precipitates were washed three times with DMF and chloroform and dried in vacuum at 150 °C for 24 h. The obtained solids were then carbonized under a nitrogen flow at 900 °C for 6 h to generate carbon nanosheets.

Preparation of carbon nanosheets-supported PdAu alloyed NCs

Typically, 10 mg of carbon nanosheets was first dispersed in 70 mL of H_2O in a round-bottom flask. Separately, the PdAu NCs (the mass ratio of metal-to-carbon is 30:70) was added into 20 mL of H_2O and stirred for 20 min. The PdAu NCs solution was then added into the carbon nanosheets solution under vigorous stirring dropwisely and sonicated for 3 h at room temperature. The solvents were then removed by vacuum filtration, and the remained solids were collected and calcined under a nitrogen flow at 600 °C for 2 h, affording a PdAu NCs/carbon nanosheets nanocomposites with a 30% total metal mass loading of PdAu. The mass loadings of the samples with different molar ratios of Au: Pd (1:0, 4:1, 2:1, 1:1, 1:2, and 0:1) were all prepared in a similar fashion, and they were denoted as Au_{100}/CNs, $Au_{80}Pd_{20}$/CNs, $Au_{67}Pd_{33}$/CNs, $Au_{50}Pd_{50}$/CNs, $Au_{33}Pd_{67}$/CNs and Pd_{100}/CNs, respectively.

Characterizations

X-ray diffraction (XRD) were detected on a Bruker D8 diffractometer with a Cu K_α radiation ($\lambda = 0.1541$ nm). The surface chemical composition of the samples were probed by X-ray photoelectron spectroscopy (XPS) by a VG Multi Lab 2000 instrument with a monochromatic Al K_α X-ray source (Thermo VG Scientific). Absorbance spectra were acquired with a Shimadzu 2600/2700 UV–visible scanning spectrophotometer. The morphology and microstructures of the samples were observed by a high-resolution transmission electron microscope (JEOL TEM-2010) equipped with an energy dispersive X-ray spectroscopy (EDS) system. The surface area was determined with a Micromeritics ASAP 2010 instrument with nitrogen adsorption at 77 K using the Barrett–Joyner–Halenda method. The pore-size distribution was calculated with a DFT method by using the nitrogen adsorption/desorption isotherm and assuming a slit pore model.

All electrochemical measurements were conducted with a CHI 750E electrochemical workstation (CH Instruments Inc.) by a standard three-electrode system at room temperature. The system is made of a glassy carbon-disk working electrode (diameter 5.61 mm, Pine Instrument Inc., RRDE collection efficiency is 37%), a AgCl/Ag reference electrode and a platinum wire as counter electrode. The working electrode was cleaned by polishing with aqueous slurries of 0.3 μm alumina powders on a microcloth. 2 mg of a catalyst was dispersed in 1.0 mL ethanol solution containing 10 μL Nafion (5 wt%, Aldrich), and the dispersion was then sonicated for 30 min to prepare a catalyst ink. Typically, 10 μL of the ink was dropcast onto the glassy carbon disk and dried at room temperature. For all catalyst samples and Pt/C, the loading was calculated as 80.8 μg cm^{-2}. All the cyclic voltammetric (CV) measurements were conducted at a scan rate of 10 mV s^{-1}, and the linear sweep voltammograms (LSV) were collected in oxygen-saturated 0.1 M KOH solution at a scan rate of 10 mV s^{-1} with different rotation rates from 100 to 2500 rpm. The durability and stability of these nanocomposite catalysts were examined by chronoamperometric measurements at +0.5 V for 30,000 s in an oxygen-saturated 0.1 M KOH solution. The rotation rate was 900 rpm. The Ag/AgCl reference electrode was calibrated with a reversible hydrogen electrode (RHE), which was performed in a high-purity H_2 (99.999%) saturated electrolyte with a Pt wire as both the working electrode and counter electrode. In 0.1 M KOH, $E_{RHE} = E_{Ag/AgCl} + 0.966$ V.

Results and discussions

Absorbance of PdAu NCs with different Pd-to-Au ratios

PdAu NCs and carbon nanosheets were prepared separately. Fig. 1 presents the Uv–vis absorbance spectra of the as-prepared clusters in water. For Au_{100}NCs, a featureless decay profile was obtained. While for Pd_{100}NCs, an absorbance band at ~420 nm can be found, which is probably due to the presence of unreacted K_2PdCl_4 (Fig. S1). Owing to the damping

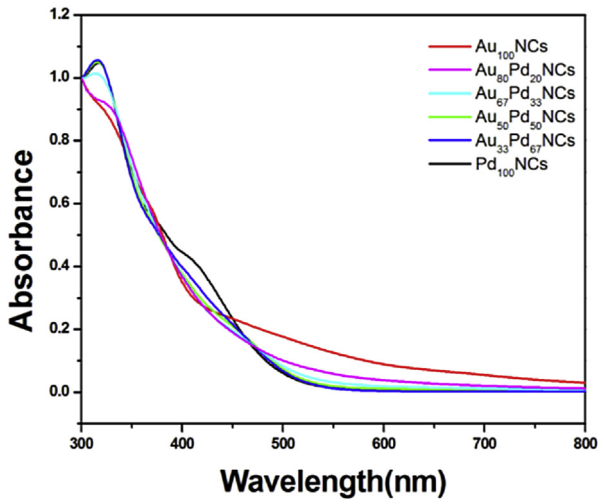

Fig. 1 – UV–visible absorbance spectra of Au_{100}, $Au_{80}Pd_{20}$, $Au_{67}Pd_{33}$, $Au_{50}Pd_{50}$, $Au_{33}Pd_{67}$, Pd_{100} alloyed nanoclusters in water.

effect of the Pd d–d transitions, Pd nanoparticles are known to exhibit no surface plasmon band in absorbance [39], while gold nanoparticles (core size larger than 2 nm) possess an typical absorbance peak at ~520 nm, thanks to their surface plasmon resonance effects [40]. With the increasing of the Pd percentage, the absorbance band at ~320 nm gradually changed into well-defined peak, and such peak can be attributed to the interaction between the tripeptide GSH and palladium surface [41]. Interestingly, for the Au_{100}NCs and all the alloyed samples, the absence of characteristic surface plasmon absorption peak at ~520 nm for gold nanoparticles indicated that the sizes of the samples are probably less than 2 nm [42,43]. It confirmed that small clusters instead of bigger nanoparticles were indeed obtained. For example, the average diameter of PdAu NCs with Pd-to-Au (1:2) is 1.4 ± 0.5 nm, as the typical TEM image and corresponding size distribution histogram are shown in Fig. S2. The representative TEM graph of carbon nanosheets can be found in Fig. S3. From nitrogen adsorption/desorption measurements (Fig. S4), the specific surface area of the carbon nanosheets was estimated to be 1046.1 $m^2 g^{-1}$ with an average pore size of 3.9 ± 0.5 nm.

TEM analysis of supported PdAu alloyed NCs

Fig. 2 shows the representative TEM images of the PdAu NCs of different ratios supported by carbon nanosheets: Au_{100}/CNs, $Au_{80}Pd_{20}$/CNs, $Au_{67}Pd_{33}$/CNs, $Au_{50}Pd_{50}$/CNs, $Au_{33}Pd_{67}$/CNs, and Pd_{100}/CNs. All the particles were evenly dispersed, and no obvious agglomeration was observed. Upon calcination, the alloyed clusters became slightly larger, and the size distribution can be found in Fig. S5. The average diameters were calculated as 2.2 ± 0.7 nm for Au_{100}/CNs, 2.4 ± 0.6 nm for $Au_{80}Pd_{20}$/CNs, 2.6 ± 0.8 nm for $Au_{67}Pd_{33}$/CNs, 2.9 ± 0.6 nm for $Au_{50}Pd_{50}$/CNs, 3.0 ± 0.9 nm for $Au_{33}Pd_{67}$/CNs, and 4.6 ± 1.5 nm for Pd_{100}/CNs. It is worth noting that, the size increased with the molecular ratio increasing of palladium, probably due to the interaction strength of Pd–S bonding is weaker than that of Au–S bonding.

To further analyze the detailed surface morphology and elemental distribution of Pd and Au, high angle annular dark field (HAADF)-STEM measurements and energy dispersive X-ray spectroscopic (EDS) mapping of $Au_{67}Pd_{33}$/CNs were conducted and shown in Fig. 3. It can be observed that the sample is highly crystalline, and the lattice fringes indicated by arrows in Fig. 3b show a d-spacing of 0.20 nm, corresponding to the (111) plane of Pd [44,45]. Both the Pd and Au species were homogeneously distributed and exhibited random elemental inter-mixing, evidenced by the Pd–Au overlapping pattern shown in Fig. 3f. The results suggest that highly homogeneous alloy catalyst supported on carbon nanosheets were obtained.

Structural analysis of PdAu alloyed CNs supported by carbon nanosheets

Next, the XRD measurements were performed to further examine the structures of the nanocomposites. As shown in Fig. 4, four additional diffraction peaks at $2\theta = 38.2°$, 44.4°, 64.6° and 77.6° were observed for Au_{100}/CNs, in agreement with the (111), (200), (220), and (311) diffractions of *fcc* gold [46]. For Pd_{100}/CNs, there were three diffraction peaks at $2\theta = 40.1°$, 46.7°, and 68.1°, in accordance with the (111), (200), and (220) diffractions of palladium [47]. For carbon nanosheets, two broad peaks can be recognized at $2\theta = 29.1$ and 42.5°, which were assigned to the (002) and (101) crystalline planes of hexagonal carbon (JCPDS 75–1621), respectively. Note that Au has sharp peaks with strong signal while Pd possesses broad peak with relatively weak signal. With the decreasing of Au amount and increasing of palladium ratio, sharp feature gradually diminished while broad feature gradually emerged. However, for all the alloyed samples, both features from Au and Pd were observed with a broadening and mixing pattern, along with the broad feature from carbon nanosheets. The results imply that Pd and Au were well intermixed and integrated with carbon nanosheets.

The chemical composition and electron charge states were then probed by XPS measurements. For the $Au_{67}Pd_{33}$ alloyed nanoclusters shown in Fig. S6, sharp peaks from Pd3d (~335 eV) and Au4f (~85 eV) electrons can be easily identified. Fig. S7 presents the XPS survey spectra of Au_{100}/CNs, $Au_{80}Pd_{20}$/CNs, $Au_{67}Pd_{33}$/CNs, $Au_{50}Pd_{50}$/CNs, $Au_{33}Pd_{67}$/CNs, and Pd_{100}/CNs. Besides the peaks of C1s (285 eV) and O1s (532 eV) from carbon nanosheets, signals from Au(4f) and Pd(3d) can be identified, indicating the successful incorporation of the alloys onto the carbon nanosheets. According to the integrated peak area, the Pd and Au contents can be determined, which are summarized in Table S1. Moreover, as shown in Fig. S8, for the samples of CNs, de-convolution of the C1s spectrum yields three peaks, sp^2 C (284.8 eV), C in C=O (285.9 eV) and C in C=O/COOH (288.5 eV); similar behaviors can be observed with the Au_{100}/CNs, $Au_{67}Pd_{33}$/CNs and Pd_{100}/CNs except that the binding energy of carbonyl/carboxylic C was about 0.4 eV, 0.3 eV and 0.2 eV lower, respectively. The results imply the formation of Au–COO^- moieties [48] in Au_{100}/CNs and $Au_{67}Pd_{33}$/CNs as well as the formation of Pd–COO^- moieties [44] in Pd_{100}/CNs and $Au_{67}Pd_{33}$/CNs. Interesting, it seems that Au has stronger interaction with carbon, as larger energy decrease (0.4 eV for Au_{100}/CNs vs 0.2 eV for Pd_{100}/CNs) was observed.

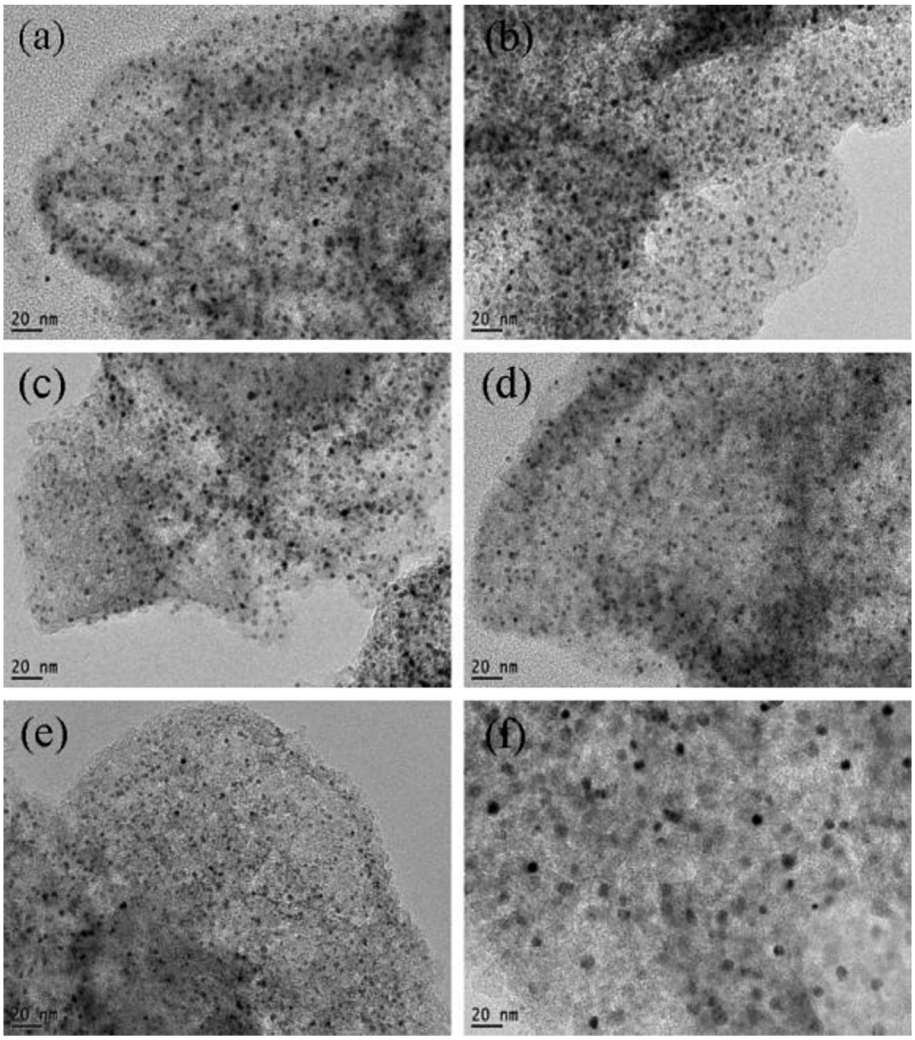

Fig. 2 – Representative TEM images of (a) Au_{100}/CNs, (b) $Au_{80}Pd_{20}$/CNs, (c) $Au_{67}Pd_{33}$/CNs, (d) $Au_{50}Pd_{50}$/CNs, (e) $Au_{33}Pd_{67}$/CNs, and (f) Pd_{100}/CNs.

RRDE measurements of PdAu/CNs samples

Interestingly, all the as-prepared nanocomposites demonstrated effective ORR activity. Fig. 5 shows the RRDE voltammograms of a glassy carbon disk electrode coated with Au_{100}/CNs, $Au_{80}Pd_{20}$/CNs, $Au_{67}Pd_{33}$/CNs, $Au_{50}Pd_{50}$/CNs, $Au_{33}Pd_{67}$/CNs, Pd_{100}/CNs as well as carbon nanosheets in a 0.1 M KOH solution saturated by O_2 with a rotation rate of 2500 rpm. For all the samples, nonzero cathodic currents started to emerge when the electrode potential was swept negatively to about +0.80–0.90 V and reached a plateau at potentials more negative than +0.60 V. However, the catalytic performance varies dramatically different with the molecular ratio variation of Pd-to-Au in the series of samples. Note that, the highest onset potential is +0.94 V from $Au_{67}Pd_{33}$/CNs, and the onset potentials of the others are estimated to be +0.89 V for Au_{100}/CNs, +0.90 V for $Au_{80}Pd_{20}$/CNs, +0.91 V for $Au_{50}Pd_{50}$/CNs, +0.90 V for $Au_{33}Pd_{67}$/CNs and +0.89 V for Pd_{100}/CNs, respectively. Meanwhile, the diffusion limited current density also exhibited a remarkable variation among the samples. The current densities were 2.94 mA cm^{-2} for Au_{100}/CNs, 4.19 mA cm^{-2} for $Au_{80}Pd_{20}$/CNs, 5.13 mA cm^{-2} for $Au_{67}Pd_{33}$/CNs, 4.08 mA cm^{-2} for $Au_{50}Pd_{50}$/CNs, 4.27 mA cm^{-2} for $Au_{33}Pd_{67}$/CNs and 4.95 mA cm^{-2} for Pd_{100}/CNs, respectively. The results indicated that, the sample of $Au_{67}Pd_{33}$/CNs exhibited the best electrocatalytic activity among the series. The results were further confirmed by the cyclic voltammetric measurements (Fig. S9).

ORR activity comparison of $Au_{67}Pd_{33}$/CNs and commercial Pt/C

Further investigation of electrocatalytic activity towards ORR of the $Au_{67}Pd_{33}$/CNs sample was then compared with commercial Pt/C by voltammetric measurements. As shown in Fig. 6a, when employing $Au_{67}Pd_{33}$/CNs or Pt/C as catalyst in N_2-saturated 0.1 M KOH solution, featureless currents without oxygen reduction peak can be observed. However, when the solution was changed into O_2-saturated 0.1 M KOH solution, a sharp cathodic peak attributed to oxygen reduction at ~0.90 V can be readily recognized. It is worth noting that, $Au_{67}Pd_{33}$/CNs exhibited an onset potential of 0.94 V vs RHE (Fig. 6b), close to that of commercial Pt/C (0.96 V). However, as shown in

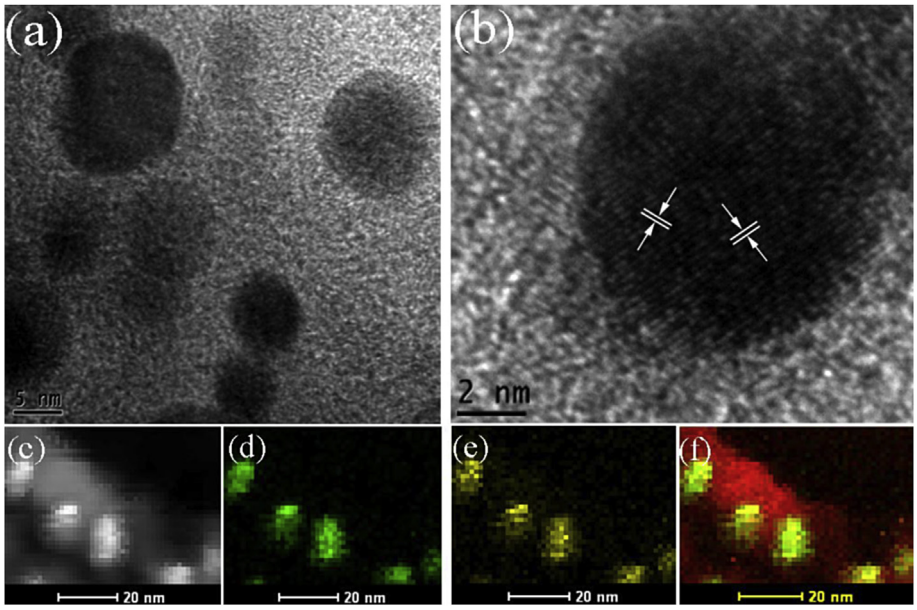

Fig. 3 – HRTEM images with different magnifications of $Au_{67}Pd_{33}$/CNs (a, b), HAADF-STEM (c), and EDS elemental mapping images of Au (d), Pd (e), and Pd–Au alloy (f). The measured d-spacing distance (arrows indicated) is approximately 0.20 nm.

Fig. 6b, the diffusion limited current density (at +0.40 V and 2500 rpm) was 5.13 mA cm^{-2} for $Au_{67}Pd_{33}$/CNs, higher than that of commercial Pt/C (4.88 mA cm^{-2}). It suggests the ORR activity of $Au_{67}Pd_{33}$/CNs was comparable with Pt/C.

Based on the RRDE data (Fig. 6b), the number of electron transfer (n) and the H_2O_2 percent yield in ORR can be calculated through the equations of

$$n = \frac{4I_d}{I_r/N + I_d} \quad (1)$$

$$H_2O_2\% = \frac{200I_r/N}{I_r/N + I_d} \quad (2)$$

where I_d is the disk current, I_r is the ring current, and N is the RRDE collection efficiency (0.37). The calculated electron transfer numbers can be found in Fig. 6c, and in the range of 0 to +0.80 V, the n values were 3.92–3.99 for $Au_{67}Pd_{33}$/CNs, higher than that of Pt/C (3.88–3.90). Meanwhile, the H_2O_2 yield for $Au_{67}Pd_{33}$/CNs was <10% in the low overpotential range of 0 to +0.80 V, less than that of Pt/C. All the above findings further confirm that $Au_{67}Pd_{33}$/CNs exhibited at least comparable, if not better, ORR activity with commercial Pt/C.

Fig. 6d presents the RRDE voltammograms of oxygen reduction recorded with the $Au_{67}Pd_{33}$/CNs coated electrode in an oxygen-saturated 0.1 M KOH solution at different rotation

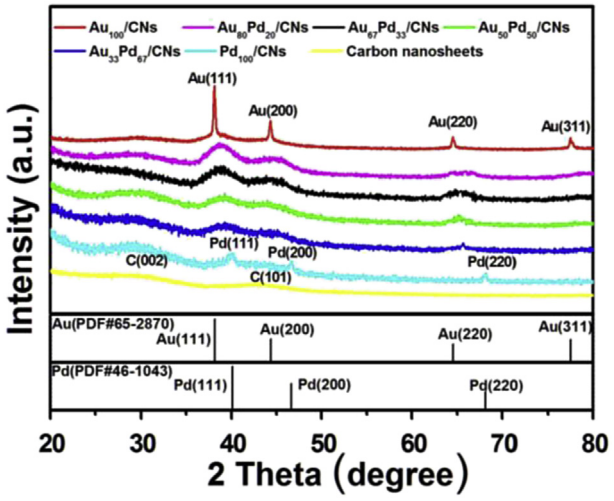

Fig. 4 – XRD patterns of Au_{100}/CNs, $Au_{80}Pd_{20}$/CNs, $Au_{67}Pd_{33}$/CNs, $Au_{50}Pd_{50}$/CNs, $Au_{33}Pd_{67}$/CNs, Pd_{100}/CNs, and carbon nanosheets.

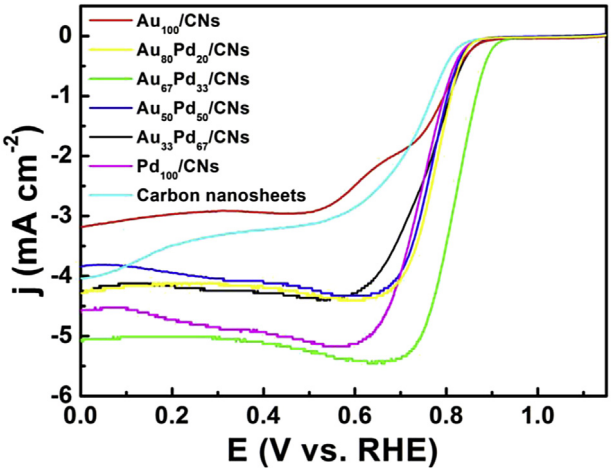

Fig. 5 – RRDE voltammograms of Au_{100}/CNs, $Au_{80}Pd_{20}$/CNs, $Au_{67}Pd_{33}$/CNs, $Au_{50}Pd_{50}$/CNs, $Au_{33}Pd_{67}$/CNs, Pd_{100}/CNs, and carbon nanosheets in O_2-saturated 0.1 M KOH at 2500 rpm.

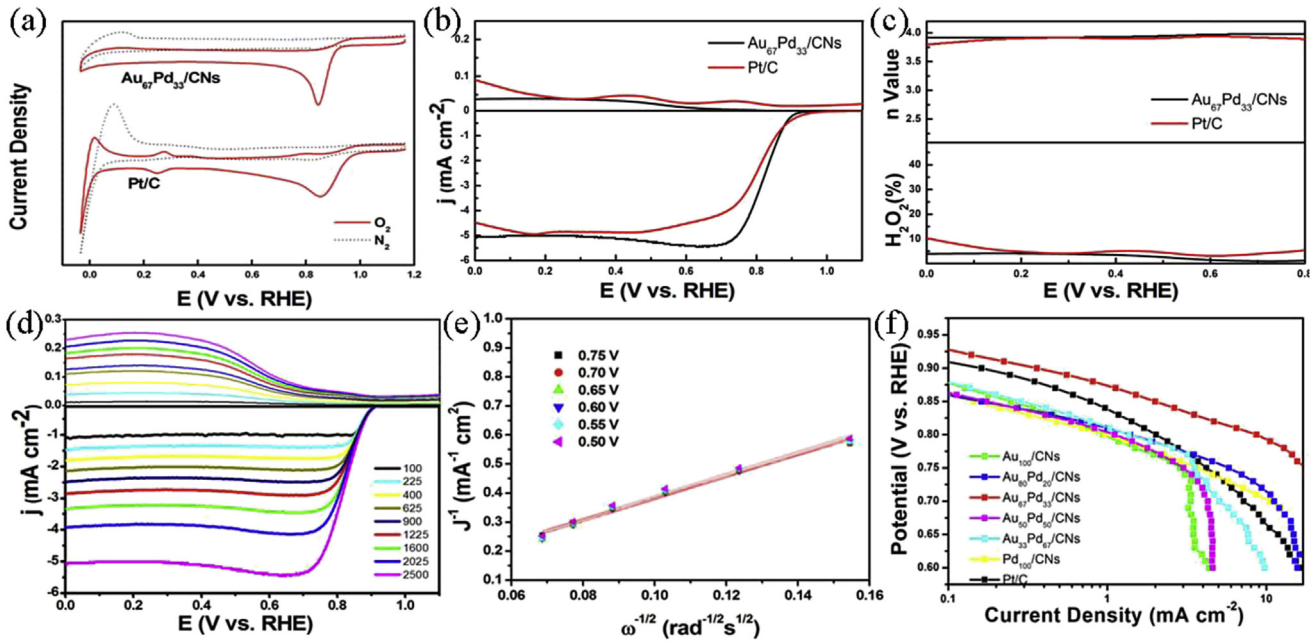

Fig. 6 – (a) Cyclic and (b) RRDE voltammograms, (c) plots of H_2O_2 yield and number of electron transfer of a glassy carbon electrode modified with $Au_{67}Pd_{33}$/CNs and commercial Pt/C catalyst in O_2-saturated 0.1 M KOH solution. Statistic results were based on data of three repeated measurements. (d) LSV curves for $Au_{67}Pd_{33}$/CNs at the rotation rates of 100–2500 rpm. (e) The corresponding K–L plots for $Au_{67}Pd_{33}$/CNs at different potentials. (f) The corresponding Tafel plots of Au_{100}/CNs, $Au_{80}Pd_{20}$/CNs, $Au_{67}Pd_{33}$/CNs, $Au_{50}Pd_{50}$/CNs, $Au_{33}Pd_{67}$/CNs, Pd_{100}/CNs and commercial 20% wt Pt/C. All measurements were tested with a catalyst loading of 80.8 μg cm^{-2} in an oxygen-saturated 0.1 M KOH aqueous solution at a potential scan rate of 10 mV s^{-1}.

rates. Apparently the voltammetric currents increased with the increasing of the rotation rate. The corresponding Koutecky–Levich (K–L) plots can be found in Fig. 6e, in the potential range from +0.50 V to 0.75 V, good linearity was acquired with a nearly identical slope. Fig. 6f depicts the corresponding Tafel plots of all the alloyed samples and Pt/C. The Tafel slopes were calculated as 67.5 mV dec^{-1} for Au_{100}/CNs, 74.1 mV dec^{-1} for $Au_{80}Pd_{20}$/CNs, 67.7 mV dec^{-1} for $Au_{67}Pd_{33}$/CNs, 62.8 mV dec^{-1} for $Au_{50}Pd_{50}$/CNs, 70.8 mV dec^{-1} for $Au_{33}Pd_{67}$/CNs, 78.3 mV dec^{-1} for Pd_{100}/CNs, and 64.4 mV dec^{-1} for Pt/C, respectively. Note that, the Tafel slope value at low current densities is generally 60 mV dec^{-1} for Pt/C coated electrode. For all the samples, the Tafel slope is in the range from 62.8 mV dec^{-1} to 74.1 mV dec^{-1}, close to that of Pt/C. The Tafel slope suggests that the rate determining step for ORR is the sluggish transfer of the first electron transfer to oxygen molecules, same with that of Pt/C.

It is worth noting that the ORR activity of the PdAu/CNs is actually superior than that of carbon nanosheets and PdAu alloys alone, as illustrated in Fig. S10. The ORR comparison of all the samples with Pt/C can be found in Table S2. In addition, with the carbon nanosheets as support, the ORR activity of $Au_{67}Pd_{33}$/CNs also outperform than recently reported alloyed samples with or without carbon support. For instances, under similar conditions, for Au–Pd alloyed nanoparticles, the cathodic peak potential is at ~−0.342 V (after calibration ~0.62 V) versus Ag/AgCl, while for Au–Pd core–shell nanoparticles, the cathodic peak potential is at ~−0.386 V (after calibration ~0.58 V), both of which are much lower than the value of the $Au_{67}Pd_{33}$/CNs sample (~0.85 V) [49]. In another study, Erikson et al. prepared PdAu alloys through an electro-deposition approach, and the best $E_{1/2}$ acquired is +0.81 V [29], which is 200 mV lower than the $Au_{67}Pd_{33}$/CNs (+0.83 V) sample in our study. These findings further demonstrate that the feasibility of the carbon support as an effective strategy to prepare supported alloyed clusters with optimized electrocatalytic performance.

The remarkable ORR activity from the supported alloyed samples might be attributed to the so-called "synergistic effects", even if the mechanism of such effects remained elusive and in debate. As for alloyed clusters, the ligand effect and ensemble effect might be the two main factors for synergistic effects [26]. The combination of two metals can significantly alter the electronic structure due to the formation of heteroatom bonds [16]. Meanwhile, palladium has strong binding to oxygenated intermediates while the introduction of a weaker binder (Au) can "dilute" that strong interaction at the atomic scale. The two effects are evidenced by the well-defined intermixing pattern observed in EDS mapping, and both of them might possess an significant impact on the electrocatalytic activity. Furthermore, carbon nanosheets might not only serve as a support, but also play a critical role in facilitating the electron transfer and mass transport behaviors

during the catalytic process [33]. All the above factors probably contributed to the enhanced activity, as dominant contributor could not be acknowledged at this level.

Furthermore, the remarkable ORR performance of the $Au_{67}Pd_{33}$/CNs sample is probably accounted for the alloying induced electronic effects. Note that, compared with Pd, Au has relatively weak bonding interactions with oxygenated species. With the introduction of gold in the alloy, the weakened interaction led to the enhanced activity with a maximum of the $Au_{67}Pd_{33}$/CNs sample, while a further increase of gold content resulted in interactions with oxygen intermediates that were too weak which diminished the ORR activity. The maximum activity of $Au_{67}Pd_{33}$/CNs sample represented the optimal balance [25]. Such perfect alloying effects can be evidenced by the HAADF-STEM images with homogeneously well-mixed Pd–Au patterns and well maintained Pd crystalline.

Durability of $Au_{67}Pd_{33}$/CNs and commercial Pt/C for ORR

Lastly, the chronoamperometric measurements were conducted to compare the durability of $Au_{67}Pd_{33}$/CNs and commercial Pt/C for ORR. As depicted in Fig. 7, after 30,000 s continuous operation, the cathodic current of the commercial Pt/C catalyst exhibited a loss of 35% of the initial value, while $Au_{67}Pd_{33}$/CNs retained about 80% (20% loss) of its initial current under the same experimental conditions. This suggests improved stability of $Au_{67}Pd_{33}$/CNs as compared to Pt/C in alkaline solution. The significant enhanced stability is probably attributed to the following factors: 1). The porous structure of the CNs not only helped prevent aggregation, dissolution and coalescence of the catalyst but also maintained electron-transport pathway for ORR [31]; 2). The mesopores of the CNs facilitated the transport of electrolyte ions, intermediates and products of the reactions [9,50]; 3). The strong electronic interaction between the carbon support and the metals (Au, Pd) was favorable for enhancing the integrity of the nanocomposite sample.

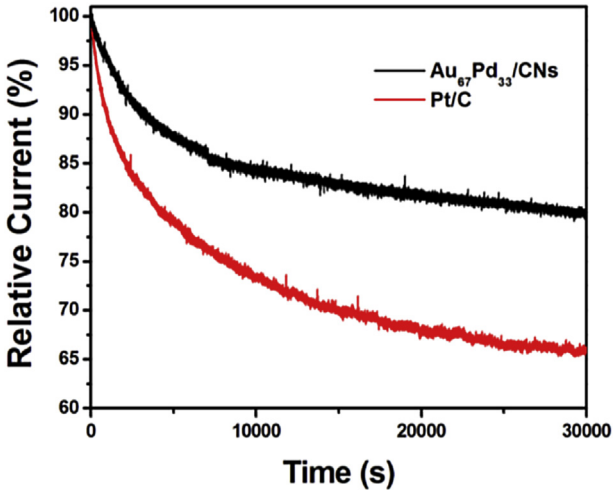

Fig. 7 – Chronoamperometric responses for ORR at $Au_{67}Pd_{33}$/CNs and Pt/C electrodes in an O_2-saturated 0.1 M KOH solution at +0.5 V for 30,000 s.

Conclusions

In summary, PdAu alloyed nanoclusters supported on carbon nanosheets were prepared and employed as efficient electrocatalysts for ORR. The hybrid materials demonstrated effective ORR activity in alkaline media. Among a series of samples, $Au_{67}Pd_{33}$/CNs stood out as the best sample, and its performance was comparable to that of commercial Pt/C while its long-term durability was markedly higher than Pt/C. The findings highlight the advantages for fabrication of alloyed nanoclusters. The carbon support strategy might be extended for the preparation of other supported bi-metallic nanoclusters with controllable composition and optimized electrocatalytic activity for fuel cell applications.

Acknowledgements

This work was supported by the National Natural Science Foundation of China (Nos. 21528301 and 21501059). Z.H.T also acknowledges financial support from the Fundamental Research Funds for the Central Universities (SCUT Grant No. 2015PT026), Guangdong Innovative and Entrepreneurial Research Team Program (No. 2014ZT05N200), and Guangdong Natural Science Funds for Distinguished Young Scholars (No. 2015A030306006). S.W.C also thanks the National Science Foundation for partial support of the work (CHE-1265635 and DMR-1409396).

Appendix A. Supplementary data

Supplementary data related to this article can be found at http://dx.doi.org/10.1016/j.ijhydene.2016.09.041.

REFERENCES

[1] Debe MK. Electrocatalyst approaches and challenges for automotive fuel cells. Nature 2012;486:43–51.
[2] Gasteiger HA, Marković NM. Just a dream or future reality. Science 2009;324:48–9.
[3] Peighambardoust SJ, Rowshanzamir S, Amjadi M. Review of the proton exchange membranes for fuel cell applications. Int J Hydrogen Energy 2010;35:9349–84.
[4] Guo S, Zhang S, Sun S. Tuning nanoparticle catalysis for the oxygen reduction reaction. Angew Chem Int Ed 2013;52:8526–44.
[5] Wu RB, Xue YH, Qian XK, Liu H, Zhou K, Chan SH, et al. Pt nanodendrites anchored on bamboo-shaped carbon nanofiber arrays as highly efficient electrocatalyst for oxygen reduction reaction. Int J Hydrogen Energy 2013;38:16677–84.
[6] Ding W, Li L, Xiong K, Wang Y, Li W, Nie Y, et al. Shape fixing via salt recrystallization: a morphology-controlled approach to convert nanostructured polymer to carbon nanomaterial as a highly active catalyst for oxygen reduction reaction. J Am Chem Soc 2015;137:5414–20.
[7] Jiao Y, Zheng Y, Jaroniec M, Qiao SZ. Design of electrocatalysts for oxygen- and hydrogen-involving energy conversion reactions. Chem Soc Rev 2015;44:2060–86.

[8] Liang H-W, Wei W, Wu Z-S, Feng X, Müllen K. Mesoporous metal–nitrogen-doped carbon electrocatalysts for highly efficient oxygen reduction reaction. J Am Chem Soc 2013;135:16002–5.
[9] Niu W, Li L, Liu X, Wang N, Liu J, Zhou W, et al. Mesoporous N-doped carbons prepared with thermally removable nanoparticle templates: an efficient electrocatalyst for oxygen reduction reaction. J Am Chem Soc 2015;137:5555–62.
[10] Cui C-H, Yu S-H. Engineering interface and surface of noble metal nanoparticle nanotubes toward enhanced catalytic activity for fuel cell applications. Acc Chem Res 2013;46:1427–37.
[11] Singh KP, Bae EJ, Yu J-S. Fe–P: a new class of electroactive catalyst for oxygen reduction reaction. J Am Chem Soc 2015;137:3165–8.
[12] Grumelli D, Wurster B, Stepanow S, Kern K. Bio-inspired nanocatalysts for the oxygen reduction reaction. Nat Commun 2013;4:2904–9.
[13] Wong WY, Daud WRW, Mohamad AB, Kadhum AAH, Loh KS, Majlan EH. Recent progress in nitrogen-doped carbon and its composites as electrocatalysts for fuel cell applications. Int J Hydrogen Energy 2013;38:9370–86.
[14] Liu K, Song Y, Chen SW. Oxygen reduction catalyzed by nanocomposites based on graphene quantum dots-supported copper nanoparticles. Int J Hydrogen Energy 2016;41:1559–67.
[15] Gao F, Goodman DW. Pd-Au bimetallic catalysts: understanding alloy effects from planar models and (supported) nanoparticles. Chem Soc Rev 2012;41:8009–20.
[16] Stamenkovic VR, Fowler B, Mun BS, Wang G, Ross PN, Lucas CA, et al. Improved oxygen reduction activity on Pt3Ni(111) via increased surface site availability. Science 2007;315:493–7.
[17] Wang C, Markovic NM, Stamenkovic VR. Advanced platinum alloy electrocatalysts for the oxygen reduction reaction. ACS Catal 2012;2:891–8.
[18] Wang C, Chi M, Li D, van der Vliet D, Wang G, Lin Q, et al. Synthesis of homogeneous Pt-bimetallic nanoparticles as highly efficient electrocatalysts. ACS Catal 2011;1:1355–9.
[19] Chung DY, Jun SW, Yoon G, Kwon SG, Shin DY, Seo P, et al. Highly durable and active PtFe nanocatalyst for electrochemical oxygen reduction reaction. J Am Chem Soc 2015;137:15478–85.
[20] Stamenkovic VR, Mun BS, Arenz M, Mayrhofer KJJ, Lucas CA, Wang G, et al. Trends in electrocatalysis on extended and nanoscale Pt-bimetallic alloy surfaces. Nat Mater 2007;6:241–7.
[21] Cortes-Escobedo CA, Gonzalez-Huerta RDG, Bolarin-Miro AM, Jesus FSD, Zhu Q, Canton SE, et al. Mechanically activated Pt-Ni and Pt-Co alloys as electrocatalysts in the oxygen reduction reaction. Int J Hydrogen Energy 2014;39:16722–30.
[22] Wu J, Shan S, Petkov V, Prasai B, Cronk H, Joseph P, et al. Composition–structure–activity relationships for palladium-alloyed nanocatalysts in oxygen reduction reaction: an ex-situ/in-situ high energy X-ray diffraction study. ACS Catal 2015;5:5317–27.
[23] Wu J, Shan S, Luo J, Joseph P, Petkov V, Zhong C-J. PdCu nanoalloy electrocatalysts in oxygen reduction reaction: role of composition and phase state in catalytic synergy. ACS Appl Mater Interfaces 2015;7:25906–13.
[24] Shao M, Odell J, Humbert M, Yu T, Xia Y. Electrocatalysis on shape-controlled palladium nanocrystals: oxygen reduction reaction and formic acid oxidation. J Phys Chem C 2013;117:4172–80.
[25] Deming CP, Zhao A, Song Y, Liu K, Khan MM, Yates VM, et al. Alkyne-protected AuPd alloy nanoparticles for electrocatalytic reduction of oxygen. ChemElectroChem 2015;2:1719–27.
[26] Paalanen P, Weckhuysen BM, Sankar M. Progress in controlling the size, composition and nanostructure of supported gold-palladium nanoparticles for catalytic applications. Catal Sci Technol 2013;3:2869–80.
[27] Devarajan S, Bera P, Sampath S. Bimetallic nanoparticles: a single step synthesis, stabilization, and characterization of Au–Ag, Au–Pd, and Au–Pt in sol–gel derived silicates. J Colloid Interface Sci 2005;290:117–29.
[28] He L-L, Song P, Feng J-J, Huang W-H, Wang Q-L, Wang A-J. Simple wet-chemical synthesis of alloyed PdAu nanochain networks with improved electrocatalytic properties. Electrochim Acta 2015;176:86–95.
[29] Erikson H, Sarapuu A, Kozlova J, Matisen L, Sammelselg V, Tammeveski K. Oxygen electroreduction on electrodeposited PdAu nanoalloys. Electrocatalysis 2015;6:77–85.
[30] Wang L, Tang Z, Liu X, Niu W, Zhou K, Yang H, et al. Ordered mesoporous carbons-supported gold nanoparticles as highly efficient electrocatalysts for oxygen reduction reaction. RSC Adv 2015;5:103421–7.
[31] Wang Q, Wang L, Tang Z, Wang F, Yan W, Yang H, et al. Oxygen reduction catalyzed by gold nanoclusters supported on carbon nanosheets. Nanoscale 2016;8:6629–35.
[32] Liu M, Zhang R, Chen W. Graphene-supported nanoelectrocatalysts for fuel cells: synthesis, properties, and applications. Chem Rev 2014;114:5117–60.
[33] Yin H, Tang H, Wang D, Gao Y, Tang Z. Facile synthesis of surfactant-free Au cluster/graphene hybrids for high-performance oxygen reduction reaction. ACS Nano 2012;6:8288–97.
[34] Morozan A, Donck S, Artero V, Gravel E, Doris E. Carbon nanotubes-gold nanohybrid as potent electrocatalyst for oxygen reduction in alkaline media. Nanoscale 2015;7:17274–7.
[35] Lin C, Song Y, Cao L, Chen S. Oxygen reduction catalyzed by Au–TiO_2 nanocomposites in alkaline media. ACS Appl Mater Interfaces 2013;5:13305–11.
[36] Negishi Y, Nobusada K, Tsukuda T. Glutathione-protected gold clusters revisited: bridging the gap between gold(I)-thiolate complexes and thiolate-protected gold nanocrystals. J Am Chem Soc 2005;127:5261–70.
[37] Ma M, Zacher D, Zhang X, Fischer RA, Metzler-Nolte NA. Method for the preparation of highly porous, nanosized crystals of isoreticular metal–organic frameworks. Cryst Growth Des 2011;11:185–9.
[38] Yoskamtorn T, Yamazoe S, Takahata R, Nishigaki J-I, Thivasasith A, Limtrakul J, et al. Thiolate-mediated selectivity control in aerobic alcohol oxidation by porous carbon-supported Au25 clusters. ACS Catal 2014;4:3696–700.
[39] Shon YS, Dawson GB, Porter M, Murray RW. Monolayer-protected bimetal cluster synthesis by core metal galvanic exchange reaction. Langmuir 2002;18:3880–5.
[40] Daniel MC, Astruc D. Gold nanoparticles: assembly, supramolecular chemistry, quantum-size-related properties, and applications toward biology, catalysis, and nanotechnology. Chem Rev 2004;104:293–346.
[41] Coppage R, Slocik JM, Sethi M, Pacardo DB, Naik RR, Knecht MR. Elucidation of peptide effects that control the activity of nanoparticles. Angew Chem Int Ed 2010;49:3767–70.
[42] Murray RW. Nanoelectrochemistry: metal nanoparticles, nanoelectrodes, and nanopores. Chem Rev 2008;108:2688–720.
[43] Varnavski O, Ramakrishna G, Kim J, Lee D, Goodson T. Critical size for the observation of quantum confinement in optically excited gold clusters. J Am Chem Soc 2010;132:16–7.
[44] Deming CP, Mercado R, Gadiraju V, Sweeney SW, Khan M, Chen S. Graphene quantum dots-supported palladium

nanoparticles for efficient electrocatalytic reduction of oxygen in alkaline media. ACS Sustain Chem Eng 2015;3:3315–23.
[45] Coppage R, Slocik JM, Briggs BD, Frenkel AI, Naik RR, Knecht MR. Determining peptide sequence effects that control the size, structure, and function of nanoparticles. ACS Nano 2012;6:1625–36.
[46] Qian H, Jin R. Controlling nanoparticles with atomic precision: the case of Au(144)(SCH(2)CH(2)Ph)(60). Nano Lett 2009;9:4083–7.
[47] Huang J, Wang D, Hou H, You T. Electrospun palladium nanoparticle-loaded carbon nanofibers and their electrocatalytic activities towards hydrogen peroxide and NADH. Adv Func Mater 2008;18:441–8.
[48] Park JW, Shumaker-Parry JS. Strong resistance of citrate anions on metal nanoparticles to desorption under thiol functionalization. ACS Nano 2015;9:1665–82.
[49] Kuai L, Yu X, Wang SZ, Sang Y, Geng BY. Au-Pd alloy and core-shell nanostructures: one-pot coreduction preparation, formation mechanism, and electrochemical properties. Langmuir 2012;28:7168–73.
[50] Liu RL, Wu DQ, Feng XL, Mullen K. Nitrogen-doped ordered mesoporous graphitic arrays with high electrocatalytic activity for oxygen reduction. Angew Chem Int Ed 2010;49:2565–9.